The influence of Fe variations on the phase stability of $CrMnFe_xCoNi$ alloys following long-duration exposures at intermediate temperatures

M. E. Bloomfield[1], K. A. Christofidou[2], F. Monni[1], Q. Yang[3], M. Hang[3], N. G. Jones[1]*

[1]Department of Materials Science and Metallurgy, University of Cambridge, 27 Charles Babbage Road, Cambridge, CB3 0FS, U.K.

[2]Department of Materials Science and Engineering, The University of Sheffield, Sir Robert Hadfield Building, Mappin Street, S1 3JD, UK

[3]School of Materials Science and Engineering, East China Jiaotong University, Nanchang, Jiangxi 330013, People's Republic of China

* ngj22@cam.ac.uk

Abstract

The equiatomic CrMnFeCoNi alloy exhibits many desirable properties, but its susceptibility to the formation of embrittling intermetallic phases, makes it unsuitable for structural applications at elevated temperatures. As a result, there is an interest in developing alternative alloys from the CrMnFeCoNi system which avoid this limitation. Here we present a detailed study of phase stability in a $CrMnFe_xCoNi$ series of alloys, where x = 0, 0.5, 1.5 (in atomic ratio), following long-duration heat treatments of 1000 h at 900 and 700˚C, and up to 5000 h at 500˚C. Each alloy was single phase *fcc* following homogenisation. After exposure at 900˚C, large σ phase precipitates were present in the CrMnCoNi alloy, but alloys containing ≥ 0.5 Fe remained single phase *fcc*. At 700˚C, the alloys investigated all contained the σ phase, Cr-*bcc* precipitates were also present in the CrMnCoNi and $CrMnFe_{0.5}CoNi$ alloys and Cr carbide precipitates featured in the $CrMnFe_{1.5}CoNi$ alloy. Heat-treatment of the CrMnCoNi alloy at 500˚C caused a partial bulk decomposition of the *fcc* matrix, which produced a fine-scale intergrowth of phases: σ, NiMn-$L1_0$, Cr-*bcc* and a secondary solute-depleted *fcc* phase. In the alloy containing 0.5 Fe, cellular regions consisting of a NiMn-$L1_0$, Cr-*bcc* and solute-depleted matrix phase, developed along the grain boundaries. NiMn-$L1_0$ and Cr-rich precipitates also formed on grain boundaries in the 1.5 Fe alloy. From these experimental observations, it was clearly established that Fe stabilises the *fcc* matrix relative to the σ and *bcc* phases.

Key words: A. High-Entropy Alloys; B. Phase stability; C. Heat treatment; D. Microstructure; E. Phase stability, prediction; F. Electron microscopy

1. Introduction

High Entropy Alloys (HEAs), which consist of multiple elements in approximately equal concentrations, occupy the centre of multi-component compositional space. This vast territory presents huge potential for the design of novel alloys, which may exhibit unique combinations of properties, suitable for multifarious applications. Among the most widely studied HEAs is the equiatomic CrMnFeCoNi alloy, which solidifies as a single *fcc* solid solution [1]. This alloy has several desirable properties, including a high fracture toughness at ambient temperatures [2], which is further enhanced with decreasing temperature to the cryogenic range [3,4]. However, its suitability for structural applications is limited due to a relatively low yield strength at ambient and elevated temperatures. Furthermore, a propensity to form embrittling intermetallic phases, including $L1_0$ and σ, during thermal exposure below ~ 800˚C [5–11], makes the alloy unsuitable for structural applications at elevated temperatures. In order to obtain desirable mechanical properties, without the susceptibility to intermetallic formation, there has been an increasing interest in developing alternative alloys based on CrMnFeCoNi [12–14]. Furthermore, various attempts have been made to tune the properties of such alloys, through the addition of other transition metal elements including V, Ti, Nb and Mo. However, this has generally resulted in the formation of deleterious intermetallic phases [15–22].

Consequently, the effective design of alloys in the CrMnFeCoNi system will require a sound understanding of the effect of composition and temperature on phase stability. However, due to the vast compositional space inherent in multi-principal component systems, the optimisation of alloy composition and processing can only reasonably be achieved through the use of predictive methods. One such method is the semi-empirical calculation of phase diagrams (CALPHAD) approach, which is capable of using thermodynamic information from unary, binary and some ternary systems to predict phase stability in higher order alloy systems. This is achieved through thermodynamic modelling and evaluation of the Gibbs energy of each phase as a function of composition, temperature and pressure. The resulting collection of optimal thermodynamic model parameters for all phases in the assessed binary and ternary systems comprises a CALPHAD database, from which thermodynamic equilibria may be calculated by a global energy minimisation procedure, allowing the construction of an equilibrium phase diagram [23–25]. However, when these predictions are extended to higher order systems, the model parameters often require adjustment to accurately describe the Gibbs energies and hence equilibrium phase stability [24]. In particular, it has been observed that

predictions often fail to accurately describe the extent to which intermetallic phases persist into multicomponent space [12,26–28]. Therefore, the use of appropriate experimental data in the development of CALPHAD databases is essential. However, due to the compositional complexity inherent in multi-principal component alloy systems, experimental reference points are few and far between. This problem is compounded by the fact that much of the phase stability data published to date, is acquired from materials which have not been subjected to appropriate homogenisation and heat-treatment steps to promote an equilibrium microstructure [29]. Furthermore, most data have been acquired from microstructures formed at temperatures above 1000˚C, where the stability of solid solution phases is greatly enhanced. As a result, CALPHAD predictions at intermediate temperatures, where intermetallic phases are more likely to form, remain largely untested. It is also important to consider that the reduced diffusivity at these temperatures, may necessitate long-duration heat-treatments to promote the precipitation of equilibrium phases. Care should also be taken to identify any precipitate phases, which may be fine-scale or occupy a small volume fraction of the alloy, by using an appropriate suite of characterisation techniques.

As mentioned above, the formation of intermetallic phases at intermediate temperatures, such as σ, can be detrimental to the mechanical properties of the CrMnFeCoNi alloy. However, with an understanding of the effect of each element on the microstructural equilibrium, the alloy composition can be tuned to supress the formation of undesirable phases. It is widely accepted that Cr is the main σ forming element in CrMnFeCoNi-based alloys [30–36], and recently, a series of detailed systematic studies have investigated the effect of Mn, Co and Ni following long-duration heat treatments at temperatures between 500 and 900˚C [12,26,27]. These studies have established that Mn promotes σ formation, whilst Co and Ni stabilise the *fcc* matrix. However, missing from the current picture is a detailed understanding of the role of Fe, which the present work seeks to address.

The Fe-free equiatomic alloy, CrMnCoNi, has been observed to form a single *fcc* phase following heat-treatment at 1000˚C for 24 h [37]. A $CrMnFe_xCoNi$ alloy containing 50 at.% Fe (with other elements in equiatomic proportions), has also been reported to be single phase *fcc* after cold rolling and subsequent 0.5 h heat-treatments between 500-800˚C, and an extended 24 h exposure at 600˚C [14]. In addition, a systematic study of $CrMnFe_xCoNi$ alloys, where x = 0-60 at.% has investigated phase stability following 2 h exposures at 900˚C [38]. Whilst X-ray diffraction (XRD) analysis indicated that each of the alloys consisted of a single *fcc* phase, microstructural characterisation, performed using scanning electron microscope (SEM)-based electron backscatter diffraction (EBSD), revealed evidence of abnormal grain

growth in the Fe-free quaternary alloy. This, the authors hypothesised, was the result of grain boundary pinning by a second phase, such as σ. In the same study, it was reported that increasing Fe-content to 80 at.% resulted in crystallisation to a single *bcc* phase, although no supporting data was published.

Considering that the σ phase is known to form in the equiatomic quinary alloy below ~ 800˚C [5–7,10,11], the aforementioned studies would suggest that increasing the Fe-content, beyond the equiatomic composition, enhances the stability of the *fcc* matrix relative to the σ phase. However, increasing the Fe-concentration also appears to reduce the stability of the *fcc* phase relative to the *bcc* phase, and above ~ 60 at.% Fe the *bcc* phase becomes dominant [38]. Thus, some insight into the influence of Fe on the microstructural equilibrium is afforded by the studies published in the literature to date. However, the relatively short heat-treatment durations employed in these studies, particularly at low homologous temperatures, may not have been sufficient to produce a detectable size / volume fraction of equilibrium phases. This is particularly important where phase characterisation was primarily conducted by XRD, which is not well suited to the detection of small volume fractions of phases. Furthermore, solidification-induced segregation could influence results where a homogenisation heat-treatment was not performed [1,28,29].

In order to establish the effect of Fe on the phase stability of $CrMnFe_xCoNi$ alloys, this paper presents a systematic study of alloys where x = 0, 0.5 and 1.5 (in atomic ratio), subjected to 1000 h thermal exposures at 900 and 700˚C, and up to 5000 h at 500˚C, to encourage an equilibrium microstructure. The resulting experimental data also facilitated the testing of equilibrium phase predictions of the TCHEA3 CALPHAD database.

2. Experimental

Ingots of three alloys, with nominal compositions CrMnCoNi, $CrMnFe_{0.5}CoNi$ and $CrMnFe_{1.5}CoNi$ (in atomic ratio), corresponding to 0, 11.1 and 27.3 at.% Fe respectively, were prepared by arc-melting of pure elements (> 99.5% purity) under an Ar atmosphere on a water-cooled Cu hearth. Each ingot was inverted and re-melted a total of 5 times to improve macroscopic homogeneity. Differential scanning calorimetry (DSC) of a small sample from the arc-melted ingots was used to determine the incipient melting temperature of each alloy as the onset of deviation from the baseline [39] (Supplementary Figure 1). A 'Netzsch DSC 404' calorimeter was used with a temperature cycle between 50 - 1450˚C at a heating/cooling rate of 10˚C / min under flowing Ar. The arc-melted ingots were then encapsulated within evacuated and Ar-backfilled quartz ampoules prior to solution heat-treatment for 100 h at 1170˚C (~ 50˚C below the lowest incipient melting temperature), followed by a rapid water quench. Transverse sections, taken from the homogenised ingots, were then re-encapsulated and heat-treated at 900, 700 and 500˚C for 1000 h and cooled by a rapid water quench. Further sections were taken from the material exposed at 500˚C, re-encapsulated and subjected to additional exposures at 500˚C, achieving total exposure durations of 2500 and 5000 h. Additional DSC was performed on each alloy in the homogenised condition to determine the alloy melting temperature.

Following heat-treatment, samples from each alloy were prepared for SEM analysis by conventional grinding and polishing using SiC paper and diamond polishing media. Final polishing was performed using a 0.04μm colloidal silica solution buffered to pH ~ 7. Microstructural characterisation was performed using Back-scattered electron (BSE) imaging in a 'Zeiss Gemini 300' SEM operated at 15 kV. Corresponding Energy Dispersive X-ray Spectroscopy (EDX) elemental partitioning maps and point/area compositions of regions of interest were generated from Kα peaks using an Oxford Instruments X-MaxN 50mm^2 silicon drift detector. The bulk composition of each alloy was determined in the homogenised condition by averaging five large area (500 × 500 μm) EDX spectra and compositional quantifications of phases were obtained by averaging at least 10 EDX spectra. The crystal structure of certain phases was also investigated by EBSD using an Oxford Instruments Symmetry detector, operated at 25 kV. The EBSD patterns were indexed using the EBSDL program [40,41] and compared with dynamical simulations, generated using the Bruker 'ESPRIT DynamicS' software. Transverse sections, ~ 1mm thick, were also taken from the

heat-treated material and prepared for XRD analysis using Ni-filtered Cu Kα radiation on a 'Bruker D8 Advance' X-ray diffractometer equipped with a 'LYNXEYE-XE' position sensitive detector. Diffraction data were acquired in the angular range 20 - 125˚ 2θ whilst the sample was rotated to improve sampling statistics. Phase identification and lattice parameters were obtained by full-pattern refinement of the XRD data using the Pawley fitting procedure [42] in TOPAS-Academic.

Further characterisation of fine-scale structures was carried out using an 'FEI Osiris' scanning transition electron microscope (STEM) equipped with 'Super-X' EDX detectors. Thin discs of material were prepared by twin-jet electropolishing using a solution of 10 wt.% $HClO_4$ in methanol at -35˚C and applied voltage of 12.5 V. In addition, lamellae containing specific regions of interest were extracted from the bulk material by focussed ion beam (FIB) milling within an FEI Helios NanoLab Dual Beam microscope. In some cases, a principal component analysis (PCA) was performed on the STEM-EDX data using HyperSpy [43]. This "machine learning" approach facilitated the identification of fine-scale and overlapping phases by separating the EDX signals from each phase according to composition.

Equilibrium phase predictions were computed using Thermo-Calc and the 'TCHEA3' thermodynamic database [25,44].

3. Results

The bulk compositions of each alloy in the homogenised condition are displayed in Table 1. The elemental concentration of each element lies within ± 1 at.% of the target concentration, except for the Mn-content of the $CrMnFe_{0.5}CoNi$ alloy, which was ~2 at.% below the target concentration. Displayed in Table 2 are the incipient melting temperatures of each alloy, determined by DSC in the homogenised condition (Supplementary Figure 1). The melting point of the alloys increased with greater Fe content, as has been reported for other alloys of the CrMnFeCoNi system [45].

It should be noted that small pores and inclusions were observed throughout the microstructures in all alloy specimens. These appeared as dark-contrast spheroidal particles in BSE images. Elemental partitioning maps, an example of which is included in Supplementary Figure 2, revealed that the inclusions were O- and Cr \ Mn-rich and depleted in Co and Ni, suggesting the presence of Cr- and Mn-based oxides.

3.1 $CrMnFe_{1.5}CoNi$

The microstructure of the $CrMnFe_{1.5}CoNi$ ($Fe_{1.5}$) alloy was characterised in the homogenised condition and following subsequent long-duration heat treatments at 900, 700 and 500˚C. Representative BSE images for each heat-treatment condition are displayed in Fig. 1. In each condition, the specimens had a large-grained microstructure with occasional annealing twins and the contrast between grains appeared to be driven by crystallographic orientation rather than compositional variations. This was confirmed by the EDX elemental partitioning maps, which showed a uniform distribution of each element in the matrix phase.

In the homogenised condition, and following exposure at 900˚C, BSE images (Fig. 1) indicated that the $CrMnFe_{1.5}CoNi$ alloy comprised a single phase, with macroscopic chemical homogeneity confirmed by EDX. However, in the 700˚C condition, precipitates with dark- and light-contrast were observed occasionally on grain boundaries. Examples of both features, along with corresponding EDX elemental partitioning maps are shown in Fig. 1. The elemental partitioning maps corresponding to the light-contrast precipitates indicated that these features were Cr-rich; depleted of Ni; slightly depleted of Mn and Fe; and had similar Co-content compared to the surrounding matrix. In contrast, the EDX data corresponding to the dark-contrast precipitates showed that these features were enriched in Cr and C, and depleted of all other elements relative to the matrix. Chemical compositions, obtained from EDX point spectra,

are displayed in Table 3. Unsurprisingly, considering the small volume fraction of precipitates, the composition of the matrix remained unchanged from the homogenised condition (Table 1). The light-contrast precipitates contained around 45 at.% Cr and were equally depleted of Mn, Fe and Co relative to the matrix, but contained only ~ 5 at.% Ni. This composition is indicative of the σ phase, which has been widely observed in alloys of the CrMnFeCoNi system [6–9,11,26,46]. The dark-contrast precipitates, on the other hand, contained ~ 70 at.% Cr and less than 10 at.% of the other elements (C was omitted from quantification as SEM-EDX is unreliable for measuring the concentration of light elements). Based on the evidence of C-enrichment in the elemental partitioning maps, the dark-contrast precipitates are thought to be a Cr-carbide phase. Three stable Cr-carbide phases have been reported in the literature: $Cr_{23}C_6$ which is *fcc*, and Cr_7C_3 and Cr_3C_2 which both have orthorhombic symmetry [47]. Among them, the $Cr_{23}C_6$ phase is most common and has previously been identified in alloys of this system, due to the intentional [48–54] and unintentional [11,12,26,27] incorporation of C. Moreover, the composition of the Cr carbide phase closely matched those of the $Cr_{23}C_6$ phase reported in the literature [12,26,27].

Following a 1000 h exposure at 500˚C, the alloy appeared to be single phase except for some very fine scale, dark-contrast grain boundary precipitates, observed in the higher magnification image of Fig. 1. A slight modulation in contrast was also observed within the grains in the higher magnification image, however, no corresponding variation in elemental partitioning was detected using EDX. As such, the difference in contrast is thought to be an artefact from chemo-mechanical polishing. The dark contrast precipitates were too fine to resolve their elemental partitioning using SEM-based EDX, so to encourage precipitate growth, the material was subjected to additional exposures at 500˚C, achieving total exposure times of 2500 h and 5000 h. After 2500 h, the grain boundary precipitates grew significantly, but little further growth had occurred after 5000 h. A higher magnification BSE image of a grain boundary region in the 5000 h condition is displayed in Fig. 2, along with corresponding EDX elemental partitioning maps. The BSE image shows a convoluted grain boundary featuring several dark-contrast precipitates. Some of these precipitates were enriched in Cr and depleted in Fe, Co and Ni relative to the matrix. Others were enriched in both Ni and Mn and depleted of all other elements relative to the matrix. A faint enrichment in the C map was also observed coincident with the Cr-rich precipitates. Based on phases previously identified in alloys of this system at 500˚C, it is likely that the phase enriched in Ni and Mn is the NiMn-$L1_0$ [6,26]. The dark-contrast Cr-rich precipitates, on the other hand, are thought to be Cr-carbides, alike those observed at 700˚C. A slight enrichment of Fe and Co could also be seen along the grain

boundaries; however, no corroboratory evidence could be obtained to suggest that this constituted an additional phase. Despite significant growth of the grain boundary precipitates after 5000 h, they remained too fine to obtain reliable chemical compositions.

XRD spectra, obtained from each alloy following homogenisation and subsequent 1000 h heat-treatments are displayed in Fig. 3. The $Fe_{1.5}$ alloy, in each condition, contained reflections corresponding to a single *fcc* phase (a = 3.60 Å), which, in the absence of any other significant phases, were attributed to the matrix phase. No reflections corresponding to the precipitate phases in the 700 and 500˚C conditions were observed. This is unsurprising, as they constituted only a very small volume fraction of the specimens, likely to be beyond the sensitivity of laboratory XRD.

3.2 $CrMnFe_{0.5}CoNi$

BSE images of the $CrMnFe_{0.5}CoNi$ ($Fe_{0.5}$) alloy following homogenisation and subsequent long-duration heat-treatments are displayed in Fig. 4. In the homogenised condition, and following subsequent exposure at 900˚C, the $Fe_{0.5}$ specimen consisted of a coarse-grained single-phase microstructure, with no evidence of second phase particles or macroscopic chemical inhomogeneity in the corresponding EDX maps (not shown). As mentioned previously, the modulated intra-granular contrast observed in certain BSE images is an artefact of chemo-mechanical polishing. Following exposure at 700˚C, BSE imaging revealed light- and dark-contrast precipitates on grain boundaries throughout the specimen. The EDX elemental partitioning maps corresponding to the dashed region, labelled (i), revealed that both the precipitate phases were enriched in Cr, but had marked differences in the partitioning of the other elements. The light-contrast phase was depleted of Mn, Ni and Fe relative to the matrix but had a similar Co-concentration, whereas the dark-contrast precipitate had a higher Cr-content than the light-contrast precipitate and was strongly depleted in all other elements relative to the matrix. In addition, neither precipitate was enriched in C. Average chemical compositions for each phase, obtained from point EDX spectra, are displayed in Table 4. Due to the small volume fraction of the precipitates, the composition of the matrix phase remained unchanged. The light-contrast precipitates contained ~50 at.% Cr, were slightly depleted of Fe and Co, and severely depleted of Mn and Ni relative to the matrix. This closely matched the partitioning behaviour of the precipitates, thought to be the σ phase, which were observed in the $Fe_{1.5}$ alloy at 700˚C. The dark-contrast phase, on the other hand, had a much greater Cr-content (~ 70 at.%) and contained < 10 at.% of the other elements. This bore close resemblance

to the Cr-based carbide phase which was identified in the $Fe_{1.5}$ alloy. However, unlike in the $Fe_{1.5}$ alloy, the elemental partitioning maps showed no evidence of C enrichment, casting doubt on their identification as Cr-carbide precipitates.

To resolve this issue, further investigations were carried out by TEM, the results of which are displayed in Fig. 5. The BSE image shows the region of the 700˚C specimen from which a lamella containing two dark-contrast precipitates was extracted by FIB milling. These precipitates are clearly seen in the High Angle Annular Dark-field (HAADF) image, near the top edge of the extracted lamella. For clarity, the grain boundary is delineated by a black-dashed line. EDX elemental partitioning maps, were obtained from the red-dashed square region of the HAADF image, which contained one of the precipitates. As with the SEM-EDX maps (Fig. 4), these data indicated that the precipitate was rich in Cr, heavily depleted of Fe, Co, and Ni, and had an intermediate Mn content. Moreover, there remained no evidence of C enrichment of the precipitate. The average composition obtained from the two precipitates, displayed in Table 4, indicated that they contained approximately 85% Cr, 8% Mn and < 3 at.% of Fe, Co and Ni. This was similar to the composition obtained from SEM-EDX. The crystal structure of the Cr-rich, dark-contrast precipitate was determined by indexing two microprobe diffraction patterns, which are inset within the HAADF image of Fig. 5. These were indexed to the [011] and [012] poles of the *bcc* crystal structure and the lattice parameter was determined to be approximately 3.0 Å. This conclusively established that the dark-contrast precipitates were the Cr-*bcc* phase, which has been reported to have a lattice parameter of ~ 2.9 Å [5,6].

Exposure at 500˚C for 1000 h resulted in the precipitation of extremely fine light- and dark-contrast phases along the grain boundaries, as shown in the BSE image displayed in Fig. 4. However, when the exposure duration was extended to 2500 h, large regions along the grain boundaries decomposed to produce a fine-scale intergrowth of light- and dark-contrast precipitates, along with a third phase of intermediate contrast. Following 5000 h at 500˚C, the decomposed regions occupied a greater volume fraction of the material than in the 2500 h condition. Elemental partitioning maps, corresponding to the dashed region of the 5000 h exposed specimen (Fig. 4), revealed that the dark-contrast precipitates were Cr-rich and depleted in all other elements relative to the matrix. Conversely, the intermediate-contrast phase was enriched in Ni & Mn, and depleted of the other elements relative to the matrix. The light-contrast phase was depleted in Mn and Ni, and had a similar Cr-, Fe- and Co-

concentration to the matrix. Although the precipitates remained too fine to obtain quantitative compositional information, it was still possible to determine their respective structures with a reasonable degree of confidence. The appearance and elemental partitioning tendencies of the Cr-rich dark-contrast phase, closely matched the Cr-*bcc*, which was identified above in the 700˚C condition (Fig. 5), and has also previously been observed at similar temperatures in the equiatomic quinary alloy [5,6]. The partitioning of Ni and Mn to the intermediate-contrast phase, on the other hand, was highly suggestive of the $L1_0$ structure. Thirdly, the light-contrast phase which surrounds the other precipitate phases in the decomposed region is thought to be a Ni- and Mn-depleted form of the *fcc* matrix, further evidence of which was to be found in the CrMnCoNi alloy at 500˚C. The existence of a second *fcc* phase, distinct in composition from the matrix, may be attributed to the rejection of solute atoms concomitant with the formation of the adjacent phases, resulting in the formation of a remnant solute depleted matrix phase.

As with the $Fe_{1.5}$ specimens, the corresponding XRD data (Fig. 3) revealed only reflections that were consistent with a single *fcc* phase (a = 3.60 Å), which is unsurprising given the small volume fraction of precipitate phases present in the 700 and 500˚C specimens.

3.3 CrMnCoNi

Representative BSE images and corresponding EDX elemental partitioning maps of the CrMnCoNi (Fe_0) alloy, following homogenisation and subsequent heat-treatments, are displayed in Fig. 6. In the homogenised condition the alloy had a large-grained single-phase microstructure, with no evidence of second phase precipitation in the BSE images or elemental partitioning maps. However, exposure of the homogenised material at 900˚C for 1000 h, resulted in the precipitation of blocky and faceted light-contrast precipitates on the grain boundaries. Blocky and needle-like precipitates, with the same light-contrast, were also observed within the grains (Supplementary Figure 2). The corresponding elemental partitioning maps, labelled (i) in Fig. 6, revealed that these light-contrast precipitates were Cr-rich and depleted of Ni and Mn, but had a similar Co-concentration to the matrix. This elemental partitioning behaviour is characteristic of the σ phase, seen previously in both the $Fe_{1.5}$ and $Fe_{0.5}$ alloys. Indeed, the quantified composition of the light-contrast phase, displayed in Table 5, closely matched that of the other σ phase precipitates (accounting for the absence of Fe). The larger size and volume fraction of σ precipitates in the Fe_0 specimen was reflected in a slight Cr-depletion of the matrix.

Heat-treatment of the Fe_0 alloy at 700˚C also resulted in the precipitation of light-contrast precipitates which were faceted and elongated along the grain boundaries and needle-like within the grains. However, these precipitates were significantly smaller than those observed at 900˚C. In addition, dark-contrast precipitates, which were finer still, were also observed along the grain boundaries. Elemental partitioning maps, corresponding to the dashed region (ii), revealed that the light-contrast precipitates exhibited elemental partitioning characteristic of the σ phase and their composition closely matched the precipitates observed in the 900˚C condition (Table 5). The elemental partitioning of the dark-contrast precipitates, on the other hand, showed an enrichment of Cr and depletion of all other alloying elements relative to the matrix. Considering the absence of any significant enrichment in C, these precipitates are likely to be the Cr-*bcc* phase, which was identified in the $Fe_{0.5}$ alloy at the same temperature (Fig. 5). Evidence that the precipitates had a *bcc* crystal structure was obtained through an analysis of their EBSD patterns. The EBSD patterns from the dark-contrast, Cr-rich precipitates in the Fe_0 and $Fe_{0.5}$ alloys are displayed in Fig. 7, alongside dynamical simulations for the *bcc* crystal structure with a lattice parameter of 2.9 Å. The experimental patterns closely matched the simulated patterns, indicating that the precipitates in the Fe_0 alloy were also Cr-*bcc*. In addition, the EBSD patterns were analysed using the EBSDL program [40,41], which showed that all the detected bands and poles could be indexed according to the *bcc* structure, with a lattice parameter between 2.8-2.9 Å.

Exposure at 500˚C for 1000 h resulted in a fine-scale decomposition of the matrix phase from the grain boundaries, which produced a complex intergrowth of ultra-fine scale precipitates (Fig. 6). SEM-EDX analysis revealed that the decomposed regions had the same bulk composition as the matrix, but the precipitates remained too fine to resolve their elemental partitioning. Following extended exposures of 2500 and 5000 h, the volume fraction of the decomposed material continued to increase. In the 5000 h condition, some precipitates had coarsened to the extent that elemental partitioning could be resolved using SEM-EDX. EDX maps, corresponding to the dashed region (iii), are displayed at the bottom of Fig. 6. These revealed three phases with distinct elemental partitioning behaviour: (1) A Cr-rich phase, which had an intermediate Co-concentration and was depleted of Mn and Ni; (2) a Co-rich phase which contained an intermediate Cr-content and was depleted of Mn and Ni; and (3) a phase rich in Ni and Mn which was depleted of Cr and Co. However, it remained impossible to resolve the elemental partitioning of the finer-scale precipitates using SEM-EDX. To characterise these ultra-fine phases, thinned regions were prepared for STEM analysis by

electropolishing. STEM-HAADF images and corresponding EDX maps of the 5000 h exposed material are displayed in Fig. 8. The HAADF images show a thinned region of the specimen which had a sponge-like, porous structure of non-uniform thickness. This made the STEM-EDX maps, corresponding to the dashed region, challenging to interpret by eye. Therefore, a principal component analysis (PCA) procedure was performed on the dataset using HyperSpy [43], which separated the EDX signal according to composition, the results of which are displayed in Fig. 9. The PCA analysis revealed the presence of 4 distinct phases: A Cr-based phase (a), a NiMn-based phase (b), and two CrCo-rich phases (c) and (d). The two CrCo-rich phases were distinguished by their Cr-content, which was substantially higher in (d). As such, the elemental partitioning tendencies of the phases identified by HyperSpy closely matched those of the larger-scale precipitates, observed by SEM-EDX (Fig. 6iii), but revealed the presence of an additional Cr-based phase (a), which did not contain a significant concentration of Co.

Quantitative compositional information from each phase, obtained from the STEM-EDX data are displayed in Table 5. The NiMn-rich precipitates contained approximately 47 at.% Ni, 41 at.% Mn and less than 10 at.% of Cr and Co respectively, as is characteristic of the NiMn $L1_0$ phase. The Cr-rich phase contained over 80 at.% Cr, which was indicative of the Cr *bcc* phase that was identified in this alloy at 700˚C. Of the two CrCo-rich phases, one contained around 48 at.% Cr, 38 at.% Co, and less than 10 at.% of Mn and Ni (Fig. 9d), while the other consisted of approximately 25 at.% Cr, 45 at.% Co, and 15 at.% of Ni and Mn (Fig. 9c). The more Cr-rich phase closely matched the elemental partitioning expected from a CrCo-based σ phase. Whereas the phase with more Co and less Cr, also had a significantly higher Ni content, which suggested that it may have an *fcc* structure.

XRD spectra, obtained from each of the CrMnCoNi specimens, are displayed in Fig. 3. In the homogenised condition, the reflections present corresponded to a single *fcc* phase (a = 3.60 Å). However, following exposure at 900˚C, in addition to the *fcc* phase, reflections characteristic of the σ phase were identified between 45-49 ˚2θ [8,15,46,55]. Furthermore, following exposure at 500˚C for 5000 h, the XRD spectra, displayed in Fig. 10, contained many additional reflections. These corresponded to two *fcc* phases (a_1 = 3.62 Å, a_2 = 3.57 Å), a σ phase (a = 8.77 Å, c = 4.53 Å), an $L1_0$ phase (a = 2.62 Å, c = 3.52 Å) and a *bcc* phase (a = 2.88 Å). This validated the identification of NiMn $L1_0$, CrCo σ, Cr *bcc* and solute-depleted *fcc* phases in the 500˚C / 5000 h condition.

4. Discussion

4.1 Effect of Fe on phase stability

The present results help to elucidate the effect of Fe on the phase stability of the $CrMnFe_xCoNi$ system. The increase of the σ solvus to over 900˚C in the CrMnCoNi alloy clearly demonstrated that increasing the Fe concentration enhances the stability of the *fcc* matrix relative to the intermetallic σ phase. This placed the σ solvus of the CrMnCoNi alloy between 900 and 1000˚C, where the alloy it has been reported to be single phase *fcc* [37]. Furthermore, the presence of intra- and inter-granular σ phase precipitates, at both 700 and 900˚C in CrMnCoNi, supported the hypothesis of Ondicho *et al.* [38], that abnormal grain coarsening was caused by the precipitation of a second phase. Our results have also revealed that increasing the Fe concentration enhanced the stability of the *fcc* matrix relative to the Cr-*bcc* phase. Cr-*bcc* precipitates were present at 700˚C in the Fe_0 and $Fe_{0.5}$ alloys, but not in the $Fe_{1.5}$ alloy. This is in good agreement with studies of the equiatomic quinary (Fe_1) alloy [6,11], which only found evidence of the Cr-*bcc* at 500˚C. It should be noted, however, that the alloy reportedly crystalises to a *bcc* solid solution when the Fe contents is above 60 at.% [38].

Based on these observations, a general hypothesis can be posited that, for alloys containing ≤ 60 at.% Fe, the *fcc* matrix is stabilised by increasing the Fe concentration. Such a hypothesis would be supported by the work of Choi *et al.* [14], which reported that alloys containing 50 at.% Fe remained single phase *fcc* following short-duration thermal exposures between 500 - 800˚C. However, further studies will be necessary to reliably establish which phases are stable in the high-Fe regime. It is also important to note, that in this study, increasing the concentration of Fe resulted in a dilution of the main σ forming element, Cr [30–36]. Therefore, as the Fe concentration is increased, a decrease in the relative stability of the σ phase is to be expected due to the dilution of Cr alone. As a result, it was not possible to isolate the effect of Fe on the stability of the σ phase.

The σ phase precipitates observed at 900 and 700˚C were often faceted, as has been observed in other alloys of the CrMnFeCoNi system [6,11,26,56], suggesting that there exists a preferred orientation relationship between the σ phase and the *fcc* matrix. This is supported by detailed investigations in superalloys and austenitic stainless steels, which have indicated that the σ phase is semi-coherent with the *fcc* lattice [57–60]. Intragranular, needle-like σ precipitates,

were also observed in the CrMnCoNi alloy, following exposure at 900 and 700˚C. Similar needle-like σ precipitates have been reported in other alloys of the CrMnFeCoNi system [26,56]. As the available evidence suggests that the σ/*fcc* interface is semi-coherent [57–60], the needle-like morphology may reduce the energy barrier for intragranular nucleation by minimising the total interfacial energy [56]. Although, it has also been proposed that that needle or plate-like σ precipitates can result from nucleation and growth along stacking faults [57].

Assessing the effect of Fe on the stability of the additional phases, which were observed at 500˚C, was considerably more challenging. At this temperature, the substitutional diffusivity is expected to control the growth of secondary phases [56,61]. Furthermore, tracer inter-diffusion studies of the CrMnCoNi and CrMnFeCoNi alloys, carried out by Dabrowa *et al.* [62], have shown that the decrease in homologous temperature with increasing Fe-concentration (Table 2), has a dominant influence on the bulk diffusivity. Therefore, it is likely that, for a given heat-treatment, the elemental diffusional distances decrease with increasing Fe-content.

In the Fe_0 and $Fe_{0.5}$ 500˚C alloy specimens, the fine-scale decomposition of the *fcc* matrix was characteristic of a discontinuous precipitation reaction [63]. This was evidenced by the cellular morphology of the decomposed regions, which developed from the grain boundaries, and the presence of a solute-depleted *fcc* phase. Due to the low bulk diffusivity at 500˚C [62], grain boundaries are likely to provide short-circuit paths for diffusion, as has been evidenced in the CrMnFeCoNi alloy [64]. In fact, a similar fine-scale decomposition on grain boundaries was observed in the CrMnFeCoNi alloy at 500˚C by Otto *et al.* [6]. Three precipitate phases (Cr-*bcc*, NiMn-$L1_0$ and FeCo-B2) were identified. However, many of the precipitates imaged in STEM, were not identified. Therefore, it is possible that a solute-depleted matrix phase was also present, leaving open the possibility of discontinuous precipitation in the CrMnFeCoNi alloy.

Among the phases which have been reported at 500˚C, the FeCo-B2 phase, which was identified by Otto *et al.* [6] in the equiatomic quinary alloy following a 12000 exposure at 500˚C, was not observed in this study. This would appear to suggest that the stability of the B2 phase is sensitive to Fe-concentration and is only stable over a narrow compositional range. However, a slight enrichment of Fe and Co was observed along the grain boundaries in the $Fe_{1.5}$ alloy at 500˚C (Fig. 2), which could allude to the eventual formation of the B2 phase. Therefore, it is possible that the formation of the B2 phase was kinetically inhibited in the $Fe_{1.5}$ alloy. It is also interesting to note, that the σ phase appeared in each alloy following heat-

treatment at 700˚C but was not observed at 500˚C, except in the CrMnCoNi alloy. It is possible that the σ phase is not thermodynamically stable at 500˚C in the Fe containing alloys. However, the absence of the σ phase could also be attributed to the slow precipitation kinetics at 500˚C, which have been predicted to delay the onset of σ phase precipitation to several thousand hours in CrMnFeCoNi alloys [61].

4.2 Fidelity of TCHEA3 predictions

The experimental data corresponding to phase stability in the $CrMnFe_xCoNi$ system, gathered here, allowed a detailed comparison to predictions made using the TCHEA3 database. Thermodynamic predictions of TCHEA3 are displayed on a pseudo-binary phase diagram in Fig. 11, where Fe is substituted equally for the other elements. The predicted solidus temperature increases linearly with increasing Fe-concentration, following the trend indicated by DSC in Table 2. However, for the Fe-containing alloys, the predicted solidus was around 20˚C higher than the measured values. Throughout the compositional range considered, a single *fcc* phase was predicted beneath the solidus. In the CrMnCoNi alloy, it is predicted that this single *fcc* region persists to ~650˚C, below which there exists a *fcc* + *bcc* two phase region. At 500˚C, the *bcc* phase is predicted for Fe-concentrations below ~7 at.% and above ~23 at.%. In contrast, the solvus of the σ phase is predicted to increase in a logarithmic manner with increasing Fe-content, reaching a plateau at around 920˚C. Thus, the database forecasts that increasing the Fe-concentration will reduce the stability of the *fcc* phase relative to the σ phase within the compositional range considered, while the effect on the *bcc* phase is less straightforward.

The experimental data points, overlaid onto the pseudo-binary phase diagram in Fig. 11, indicate the phases that have been experimentally observed in this study, and in previous studies of the CrMnFeCoNi alloy involving long-duration heat-treatments [6,11]. Green squares denote compositions which were single phase *fcc*, red circles for those which additionally contained σ phase precipitates, purple hexagons for those containing σ and *bcc* precipitates, and blue diamond's where other phases were present. Whilst TCHEA3 predicted that the σ solvus would increase with Fe-concentration, the experimental results indicated the reverse trend. In the CrMnCoNi alloy, the σ phase was observed following heat-treatment at 900˚C, despite its solvus being predicted to drop precipitously with decreasing Fe, to below 400˚C at ~ 2 at.% Fe. Furthermore, the alloys containing Fe were all single phase *fcc* at 900˚C,

but exhibited σ precipitates at 700˚C, indicating a suppression of the σ solvus as the Fe concentration was increased.

The Cr-*bcc* phase, on the other hand, was observed at 700˚C in the Fe_0 alloy, significantly above its predicted solvus temperature of ~ 645˚C. Cr-*bcc* precipitates were also identified outside of the predicted *bcc* phase field in the $Fe_{0.5}$ alloy, at 700 and 500˚C. In addition, the *bcc* phase has been identified in the Fe_1 at 500˚C [6]. As such, it appears that the extent of the *bcc* phase field in the low Fe region of the phase diagram extends to higher temperatures and Fe concentrations than predicted by TCHEA3. The database also predicted a low temperature *bcc* phase field at Fe concentrations > 15 at.%, which included the $Fe_{1.5}$ alloy at 500˚C. Accordingly#, it should be noted that the dark-contrast Cr-rich precipitates observed in this alloy condition, which were assumed to be Cr carbides, could also be characteristic of the Cr-*bcc* phase. However, a precise identification of the structure of theses precipitates was not possible due to their small size and extremely low volume fraction.

Missing from the TCHEA3 predictions was the FeCo-B2 phase, which has been reported in the Fe_1 alloy at 500˚C [5,6,10]. Also, as previously discussed, there was some evidence of Fe and Co co-partitioning along grain boundaries in the $Fe_{1.5}$ alloy at 500˚C. Another phase, entirely missing from the predictions of TCHEA3, was the NiMn-$L1_0$, which was present at 500˚C in all the alloys investigated. In fact, the NiMn-$L1_0$ phase is notable in its absence from thermodynamic predictions in the CrMnFeCoNi system using the TCHEA databases [26,44]. It has been suggested that this may be due to the simplified 2-sublattice model, used to describe the $L1_0$ phase, which assumes a pure binary phase containing an equal fraction of each element [44]. This is at odds with experimental compositional measurements of the $L1_0$ phase, published here (Table 5), and in previous studies [6,26], which suggest that a finite amount of Cr, Co and Fe are soluble within the $L1_0$ structure. Accordingly, the stability of the $L1_0$ phase, predicted by TCHEA3, may be enhanced by considering the solubility of these elements, through the application of a 4-sublattice partitioning model. With this in mind, it is interesting to note that TCHEA3 predicted a NiMn-B2 phase below 500˚C at low Fe-concentrations. To the knowledge of the present authors, such a phase has not been observed experimentally in the CrMnFeCoNi system. Therefore, it is possible that a reduction in the predicted stability of the $L1_0$ phase, due to the limitations of the 2-sublattice model, has resulted in the erroneous prediction of a NiMn-B2 phase.

It should be noted that thermodynamic calculations were preformed using nominal alloy chemistries, which deviated slightly from the experimentally achieved compositions (Table 1). In addition, the presence of C contamination was not accounted for in the thermodynamic calculations. As a result, the presence of carbide precipitates has been ignored when comparing experimental results with TCHEA3 predictions.

5. Conclusions

In this study, the effect of Fe concentration on the phase stability of a $CrMnFe_xCoNi$ family of alloys was experimentally investigated. This facilitated an assessment of the fidelity of equilibrium phase predictions of the TCHEA3 thermodynamic database.

The results show that increasing the Fe concentration stabilised the *fcc* matrix phase relative to the Cr-rich σ and *bcc* phases. The σ phase was identified in the Fe_0 alloy following thermal exposure at 900˚C, but with the addition of Fe its solvus temperature was depressed to below 900˚C. Analogously, the *bcc* phase was observed at 700˚C in both the Fe_0 and $Fe_{0.5}$ alloys but has only been reported at 500˚C in the equiatomic CrMnFeCoNi alloy. Further decomposition of the *fcc* matrix at 500˚C, resulted in the formation of multiple intermetallic phases in each alloy. In the Fe_0 alloy, a partial bulk decomposition of the *fcc* matrix, which was characteristic of discontinuous precipitation, produced a fine-scale intergrowth of σ, NiMn-$L1_0$, Cr-*bcc*, and solute-depleted *fcc* phases. Similarly, in the $Fe_{0.5}$ alloy, cellular regions containing a NiMn-$L1_0$, solute-depleted *fcc* and Cr-*bcc* phase developed along the grain boundaries, in a manner which was also characteristic of discontinuous precipitation. Lastly, NiMn-$L1_0$ and Cr-rich precipitates, believed to be Cr carbides, were observed on the grain boundaries of the $Fe_{1.5}$ alloy.

A comparison of experimental results with thermodynamic predictions, confuted the prediction that the σ solvus would rise with increasing Fe-concentration. Furthermore, in the low Fe regime, the *bcc* phase field was found to extend to higher temperatures and Fe concentrations than predicted. In addition, the predictions omitted the NiMn-$L1_0$ phase, which formed in all of the alloys at 500˚C, as well as the FeCo-B2 phase, which has been reported in the CrMnFeCoNi alloy. To summarise, the TCHEA3 database was able to predict most of the phases observed experimentally but the temperature and composition range over which these phases existed was not accurately described. It is hoped that further optimisation of the thermodynamic database, using the data presented in this paper, will enable reliable predictions of phase stability in this system.

Acknowledgements

The authors would like to thank S. Rhodes, H.T. Pang and G. Divitini for their invaluable assistance and helpful discussions. The authors acknowledge support from the Rolls-Royce / EPSRC Strategic Partnership [grant number EP/M005607/1]. The underlying data from this work can be found in the University of Cambridge data repository: www.data.cam.ac.uk

References

[1] D.B. Miracle, O.N. Senkov, A critical review of high entropy alloys and related concepts, Acta Mater. 122 (2017) 448–511. doi:10.1016/j.actamat.2016.08.081.

[2] B. Gludovatz, A. Hohenwarter, D. Catoor, E.H. Chang, E.P. George, R.O. Ritchie, A fracture-resistant high-entropy alloy for cryogenic applications, Science (80-.). 345 (2014) 1153–1158. doi:10.1126/science.1254581.

[3] A. Gali, E.P. George, Tensile properties of high- and medium-entropy alloys, Intermetallics. 39 (2013) 74–78. doi:10.1016/j.intermet.2013.03.018.

[4] F. Otto, A. Dlouhý, C. Somsen, H. Bei, G. Eggeler, E.P.P. George, The influences of temperature and microstructure on the tensile properties of a CoCrFeMnNi high-entropy alloy, Acta Mater. 61 (2013) 5743–5755. doi:10.1016/j.actamat.2013.06.018.

[5] B. Schuh, F. Mendez-Martin, B. Völker, E.P. George, H. Clemens, R. Pippan, A. Hohenwarter, Mechanical properties, microstructure and thermal stability of a nanocrystalline CoCrFeMnNi high-entropy alloy after severe plastic deformation, Acta Mater. 96 (2015) 258–268. doi:10.1016/j.actamat.2015.06.025.

[6] F. Otto, A. Dlouhý, K.G. Pradeep, M. Kuběnová, D. Raabe, G. Eggeler, E.P. George, Decomposition of the single-phase high-entropy alloy CrMnFeCoNi after prolonged anneals at intermediate temperatures, Acta Mater. 112 (2016) 40–52. doi:10.1016/j.actamat.2016.04.005.

[7] N.D. Stepanov, D.G. Shaysultanov, M.S. Ozerov, S. V. Zherebtsov, G.A. Salishchev, Second phase formation in the CoCrFeNiMn high entropy alloy after recrystallization annealing, Mater. Lett. 185 (2016) 1–4. doi:10.1016/j.matlet.2016.08.088.

[8] W. Zhou, L.M.M. Fu, P. Liu, X.D.D. Xu, B. Chen, G.Z.Z. Zhu, X.D.D. Wang, A.D.D. Shan, M.W.W. Chen, Deformation stimulated precipitation of a single-phase CoCrFeMnNi high entropy alloy, Intermetallics. 85 (2017) 90–97.

doi:10.1016/J.INTERMET.2017.02.010.

[9] M.V. Klimova, D.G. Shaysultanov, S.V. Zherebtsov, N.D. Stepanov, Effect of second phase particles on mechanical properties and grain growth in a CoCrFeMnNi high entropy alloy, Mater. Sci. Eng. A. 748 (2019) 228–235. doi:10.1016/J.MSEA.2019.01.112.

[10] K.H. Lee, S.-K. Hong, S.I. Hong, Precipitation and decomposition in CoCrFeMnNi high entropy alloy at intermediate temperatures under creep conditions, Materialia. 8 (2019) 100445. doi:10.1016/J.MTLA.2019.100445.

[11] E.J. Pickering, R. Muñoz-Moreno, H.J. Stone, N.G. Jones, Precipitation in the equiatomic high-entropy alloy CrMnFeCoNi, Scr. Mater. 113 (2016) 106–109. doi:10.1016/j.scriptamat.2015.10.025.

[12] K.A. Christofidou, T.P. McAuliffe, P.M. Mignanelli, H.J. Stone, N.G. Jones, On the prediction and the formation of the sigma phase in CrMnCoFeNi x high entropy alloys, J. Alloys Compd. 770 (2018) 285–293. doi:10.1016/j.jallcom.2018.08.032.

[13] G.A. Salishchev, M.A. Tikhonovsky, D.G. Shaysultanov, N.D. Stepanov, A.V. Kuznetsov, I.V. Kolodiy, A.S. Tortika, O.N. Senkov, Effect of Mn and V on structure and mechanical properties of high-entropy alloys based on CoCrFeNi system, J. Alloys Compd. 591 (2014) 11–21. doi:10.1016/j.jallcom.2013.12.210.

[14] M. Choi, I. Ondicho, N. Park, N. Tsuji, Strength–ductility balance in an ultrafine-grained non-equiatomic Fe50(CoCrMnNi)50 medium-entropy alloy with a fully recrystallized microstructure, J. Alloys Compd. 780 (2019) 959–966. doi:10.1016/J.JALLCOM.2018.11.265.

[15] N.D. Stepanov, D.G. Shaysultanov, G.A. Salishchev, M.A. Tikhonovsky, E.E. Oleynik, A.S. Tortika, O.N. Senkov, Effect of v content on microstructure and mechanical properties of the CoCrFeMnNiVx high entropy alloys, J. Alloys Compd. 628 (2015) 170–185. doi:10.1016/j.jallcom.2014.12.157.

[16] M.-H. Chuang, M.-H. Tsai, W.-R. Wang, S.-J. Lin, J.-W. Yeh, Microstructure and wear behavior of AlxCo1.5CrFeNi1.5Tiy high-entropy alloys, Acta Mater. 59 (2011) 6308–6317. doi:10.1016/J.ACTAMAT.2011.06.041.

[17] W.H. Liu, J.Y. He, H.L. Huang, H. Wang, Z.P. Lu, C.T. Liu, Effects of Nb additions on the microstructure and mechanical property of CoCrFeNi high-entropy alloys, Intermetallics. 60 (2015) 1–8. doi:10.1016/J.INTERMET.2015.01.004.

[18] W.H. Liu, Z.P. Lu, J.Y. He, J.H. Luan, Z.J. Wang, B. Liu, Y. Liu, M.W. Chen, C.T. Liu, Ductile CoCrFeNiMox high entropy alloys strengthened by hard intermetallic

phases, Acta Mater. 116 (2016) 332–342. doi:10.1016/J.ACTAMAT.2016.06.063.

[19] M. Detrois, S. Antonov, S. Tin, Phase stability and thermodynamic database validation in a set of non-equiatomic Al-Co-Cr-Fe-Nb-Ni high-entropy alloys, Intermetallics. 104 (2019) 103–112. doi:10.1016/J.INTERMET.2018.11.002.

[20] T.-T. Shun, L.-Y. Chang, M.-H. Shiu, Microstructure and mechanical properties of multiprincipal component CoCrFeNiMox alloys, Mater. Charact. 70 (2012) 63–67. doi:10.1016/J.MATCHAR.2012.05.005.

[21] C.-H. Tsau, M.-C. Tsai, The Effects of Mo and Nb on the Microstructures and Properties of CrFeCoNi(Nb,Mo) Alloys, Entropy. 20 (2018) 648. doi:10.3390/e20090648.

[22] J. Miller, Microstructural and Mechanical Effects of Refractory Metal Additions to 3d Transition Metal High Entropy Alloys, University of Cambridge, 2019.

[23] N. (Nigel) Saunders, N. Saunders, CALPHAD : calculation of phase diagrams : a comprehensive guide / by N. Saunders and A.P. Miodownik., Pergamon, London, 1998.

[24] H. Lukas, S. Fries, B. Sundman, Computational thermodynamics: The Calphad Method, Cambridge University Press, Cambridge, 2007.

[25] H. Mao, H.-L. Chen, Q. Chen, TCHEA1: A Thermodynamic Database Not Limited for “High Entropy” Alloys, J. Phase Equilibria Diffus. 38 (2017) 353–368. doi:10.1007/s11669-017-0570-7.

[26] M.E. Bloomfield, K.A. Christofidou, N.G. Jones, Effect of Co on the phase stability of CrMnFeCoxNi high entropy alloys following long-duration exposures at intermediate temperatures, Intermetallics. 114 (2019) 106582. doi:10.1016/J.INTERMET.2019.106582.

[27] K.A. Christofidou, E.J. Pickering, P. Orsatti, P.M. Mignanelli, T.J.A. Slater, H.J. Stone, N.G. Jones, On the influence of Mn on the phase stability of the CrMn x FeCoNi high entropy alloys, Intermetallics. 92 (2018) 84–92. doi:10.1016/j.intermet.2017.09.011.

[28] F. Zhang, C. Zhang, S.L. Chen, J. Zhu, W.S. Cao, U.R. Kattner, An understanding of high entropy alloys from phase diagram calculations, Calphad. 45 (2014) 1–10. doi:10.1016/J.CALPHAD.2013.10.006.

[29] E.J. Pickering, N.G. Jones, High-entropy alloys: a critical assessment of their founding principles and future prospects, Int. Mater. Rev. 61 (2016) 183–202. doi:10.1080/09506608.2016.1180020.

[30] A.S. Wilson, Formation and effect of topologically close-packed phases in nickel-base superalloys, Mater. Sci. Technol. 33 (2017) 1108–1118. doi:10.1080/02670836.2016.1187335.

[31] A.J. Zaddach, R.O. Scattergood, C.C. Koch, Tensile properties of low-stacking fault energy high-entropy alloys, Mater. Sci. Eng. A. 636 (2015) 373–378. doi:10.1016/J.MSEA.2015.03.109.

[32] G. Bracq, M. Laurent-Brocq, L. Perrière, R. Pirès, J.-M. Joubert, I. Guillot, The fcc solid solution stability in the Co-Cr-Fe-Mn-Ni multi-component system, Acta Mater. 128 (2017) 327–336. doi:10.1016/j.actamat.2017.02.017.

[33] K. Ming, X. Bi, J. Wang, Microstructures and deformation mechanisms of Cr26Mn20Fe20Co20Ni14alloys, Mater. Charact. 134 (2017) 194–201. doi:10.1016/j.matchar.2017.10.022.

[34] M.-H. Tsai, K.-Y. Tsai, C. Tsai, C. Lee, C.-C. Juan, J.-W. Yeh, Criterion for Sigma Phase Formation in Cr- and V-Containing High-Entropy Alloys, Mater. Res. Lett. 1 (2013) 207–212. doi:10.1080/21663831.2013.831382.

[35] M.-H. Tsai, K.-C. Chang, J.-H. Li, R.-C. Tsai, A.-H. Cheng, A second criterion for sigma phase formation in high-entropy alloys, Mater. Res. Lett. 4 (2016) 90–95. doi:10.1080/21663831.2015.1121168.

[36] N.D. Stepanov, D.G. Shaysultanov, M.A. Tikhonovsky, G.A. Salishchev, Tensile properties of the Cr-Fe-Ni-Mn non-equiatomic multicomponent alloys with different Cr contents, Mater. Des. 87 (2015) 60–65. doi:10.1016/j.matdes.2015.08.007.

[37] K. Guruvidyathri, B.S. Murty, J.W. Yeh, K.C. Hari Kumar, Gibbs energy-composition plots as a tool for high-entropy alloy design, J. Alloys Compd. 768 (2018) 358–367. doi:10.1016/J.JALLCOM.2018.07.264.

[38] I. Ondicho, M. Choi, W.-M. Choi, J.B. Jeon, H.R. Jafarian, B.-J. Lee, S.I. Hong, N. Park, Experimental investigation and phase diagram of CoCrMnNi–Fe system bridging high-entropy alloys and high-alloyed steels, J. Alloys Compd. 785 (2019) 320–327. doi:10.1016/J.JALLCOM.2019.01.134.

[39] W.J. Boettinger, U.R. Kattner, J.H. Perepezko, DTA and Heat-flux DSC Measurements of Alloy Melting and Freezing, 2006. https://www.nist.gov/publications/nist-recommended-practice-guide-dta-and-heat-flux-dsc-measurements-alloy-melting-and.

[40] L. Li, S. Ouyang, Y. Yang, M. Han, EBSDL : a computer program for determining an unknown Bravais lattice using a single electron backscatter diffraction pattern, J. Appl.

Crystallogr. 47 (2014) 1466–1468. doi:10.1107/S160057671401382X.

[41] M. Han, C. Chen, G. Zhao, L. Li, G. Nolze, B. Yu, X. Huang, Y. Zhu, Blind lattice-parameter determination of cubic and tetragonal phases with high accuracy using a single EBSD pattern, Acta Crystallogr. Sect. A Found. Adv. 74 (2018) 630–639. doi:10.1107/S2053273318010963.

[42] G.S. Pawley, Unit-cell refinement from powder diffraction scans, J. Appl. Crystallogr. 14 (1981) 357–361. doi:10.1107/S0021889881009618.

[43] F. de la Peña, E. Prestat, V.T. Fauske, P. Burdet, P. Jokubauskas, M. Nord, T. Ostasevicius, K.E. MacArthur, M. Sarahan, D.N. Johnstone, J. Taillon, J. Lähnemann, V. Migunov, A. Eljarrat, J. Caron, T. Aarholt, S. Mazzucco, M. Walls, T. Slater, F. Winkler, B. Martineau, G. Donval, R. McLeod, E.R. Hoglund, I. Alxneit, D. Lundeby, T. Henninen, L.F. Zagonel, A. Garmannslund, hyperspy/hyperspy: HyperSpy v1.5.2, (2019). doi:10.5281/ZENODO.3396791.

[44] H.-L. Chen, H. Mao, Q. Chen, Database development and Calphad calculations for high entropy alloys: Challenges, strategies, and tips, Mater. Chem. Phys. 210 (2018) 279–290. doi:10.1016/j.matchemphys.2017.07.082.

[45] D. Ma, M. Yao, K.G. Pradeep, C.C. Tasan, H. Springer, D. Raabe, Phase stability of non-equiatomic CoCrFeMnNi high entropy alloys, Acta Mater. 98 (2015) 288–296. doi:10.1016/j.actamat.2015.07.030.

[46] Z.G. Zhu, K.H. Ma, X. Yang, C.H. Shek, Annealing effect on the phase stability and mechanical properties of (FeNiCrMn) (100−x) Co x high entropy alloys, J. Alloys Compd. 695 (2017) 2945–2950. doi:10.1016/j.jallcom.2016.11.376.

[47] A. Ganguly, V. Murthy, K. Kannoorpatti, Structural and electronic properties of chromium carbides and Fe-substituted chromium carbides, Mater. Res. Express. 7 (2020) 056508. doi:10.1088/2053-1591/ab8cf9.

[48] J. PENG, Z. yong LI, X. bo JI, Y. le SUN, L. ming FU, A. dang SHAN, Decomposition kinetics of carbon-doped FeCoCrNiMn high-entropy alloy at intermediate temperature, Trans. Nonferrous Met. Soc. China (English Ed. 30 (2020) 1884–1894. doi:10.1016/S1003-6326(20)65347-X.

[49] M. Klimova, D. Shaysultanov, A. Semenyuk, S. Zherebtsov, N. Stepanov, Effect of carbon on recrystallised microstructures and properties of CoCrFeMnNi-type high-entropy alloys, J. Alloys Compd. 851 (2020) 156839. doi:10.1016/j.jallcom.2020.156839.

[50] L. Guo, X. Ou, S. Ni, Y. Liu, M. Song, Effects of carbon on the microstructures and

mechanical properties of FeCoCrNiMn high entropy alloys, Mater. Sci. Eng. A. 746 (2019) 356–362. doi:10.1016/j.msea.2019.01.050.

[51] J. Li, B. Gao, S. Tang, B. Liu, Y. Liu, Y. Wang, J. Wang, High temperature deformation behavior of carbon-containing FeCoCrNiMn high entropy alloy, J. Alloys Compd. 747 (2018) 571–579. doi:10.1016/J.JALLCOM.2018.02.332.

[52] N.D. Stepanov, N.Y. Yurchenko, M.A. Tikhonovsky, G.A. Salishchev, Effect of carbon content and annealing on structure and hardness of the CoCrFeNiMn-based high entropy alloys, J. Alloys Compd. 687 (2016) 59–71. doi:10.1016/J.JALLCOM.2016.06.103.

[53] H. Cheng, H.Y. Wang, Y.C. Xie, Q.H. Tang, P.Q. Dai, Controllable fabrication of a carbide-containing FeCoCrNiMn high-entropy alloy: microstructure and mechanical properties, Mater. Sci. Technol. 33 (2017) 2032–2039. doi:10.1080/02670836.2017.1342367.

[54] N.D. Stepanov, D.G. Shaysultanov, R.S. Chernichenko, N.Y. Yurchenko, S. V. Zherebtsov, M.A. Tikhonovsky, G.A. Salishchev, Effect of thermomechanical processing on microstructure and mechanical properties of the carbon-containing CoCrFeNiMn high entropy alloy, J. Alloys Compd. 693 (2017) 394–405. doi:10.1016/j.jallcom.2016.09.208.

[55] N. Park, B.-J. Lee, N. Tsuji, The phase stability of equiatomic CoCrFeMnNi high-entropy alloy: Comparison between experiment and calculation results, J. Alloys Compd. 719 (2017) 189–193. doi:10.1016/J.JALLCOM.2017.05.175.

[56] G. Laplanche, Growth Kinetics of Σ-Phase Precipitates and Underlying Diffusion Processes in Crmnfeconi High-Entropy Alloys, SSRN Electron. J. (2020). doi:10.2139/ssrn.3592043.

[57] S. Nenno, M. Tagaya, K. Hosomi, Z. Nishiyama, Electron Microscope Study of Sigma Phase Precipitation in an Iron-Chromium-Nickel Alloy, Trans. Japan Inst. Met. 4 (1963) 222–230. doi:10.2320/matertrans1960.4.222.

[58] M.H. Lewis, Precipitation of (Fe, Cr) sigma phase from austenite, Acta Metall. 14 (1966) 1421–1428. doi:10.1016/0001-6160(66)90162-3.

[59] WEISS B, STICKLER R, Phase instabilities during high temperature exposure of 316 austenitic stainless steel, Met Trans. 3 (1972) 851–866. doi:10.1007/bf02647659.

[60] C.M.F. Rae, R.C. Reed, The precipitation of topologically close-packed phases in rhenium-containing superalloys, Acta Mater. 49 (2001) 4113–4125. doi:10.1016/S1359-6454(01)00265-8.

[61] G. Laplanche, S. Berglund, C. Reinhart, A. Kostka, F. Fox, E.P. George, Phase stability and kinetics of σ-phase precipitation in CrMnFeCoNi high-entropy alloys, Acta Mater. 161 (2018) 338–351. doi:10.1016/J.ACTAMAT.2018.09.040.

[62] J. Dąbrowa, M. Zajusz, W. Kucza, G. Cieślak, K. Berent, T. Czeppe, T. Kulik, M. Danielewski, Demystifying the sluggish diffusion effect in high entropy alloys, J. Alloys Compd. 783 (2019) 193–207. doi:10.1016/j.jallcom.2018.12.300.

[63] I. Manna, S.K. Pabi, W. Gust, Discontinuous reactions in solids, Int. Mater. Rev. 46 (2001) 53–91. doi:10.1179/095066001101528402.

[64] M. Glienke, M. Vaidya, K. Gururaj, L. Daum, B. Tas, L. Rogal, K.G. Pradeep, G. Wilde, S. V. Divinski, Grain boundary diffusion in CoCrFeMnNi high entropy alloy: kinetic hints towards a phase decomposition, Acta Mater. 195 (2020) 304–316. doi:10.1016/j.actamat.2020.05.009.

Table 1
Bulk compositions of each alloy in the homogenised condition, obtained from the average of five large area EDX scans. The elemental concentrations are quoted in atomic percent and the error is the standard deviation between the measurements.

Alloy	Cr	Mn	Fe	Co	Ni
$CrMnFe_{1.5}CoNi$	18.5 ± 0.1	18.2 ± 0.2	27.2 ± 0.1	18.2 ± 0.2	17.9 ± 0.1
$CrMnFe_{0.5}CoNi$	23.0 ± 0.1	20.4 ± 0.1	11.4 ± 0.1	22.6 ± 0.1	22.6 ± 0.1
CrMnCoNi	25.5 ± 0.1	25.0 ± 0.1	-	24.9 ± 0.1	24.6 ± 0.1

Table 2
Solidus temperatures obtained from DSC of alloys in the homogenised condition. The solidus was taken as the onset of melting during heating at 10˚C / min.

Alloy	DSC Solidus (˚C)
$CrMnFe_{1.5}CoNi$	1305
$CrMnFe_{0.5}CoNi$	1265
CrMnFeNi	1215

Table 3

Phase compositions of the $CrMnFe_{1.5}CoNi$ alloy following a 1000 h heat treatment at 700˚C, obtained by averaging of point EDX spectra. Elemental concentrations are given in at. %, along with the standard deviation between the measurements.

Condition	Phase / structure	Cr	Mn	Fe	Co	Ni
700°C	matrix / *fcc*	18.7 ± 0.1	18.1 ± 0.3	26.9 ± 0.3	18.6 ± 0.3	17.7 ± 0.2
	light ppt. / σ	44.3 ± 0.8	13.0 ± 0.3	22.0 ± 0.2	15.3 ± 0.3	5.4 ± 0.4
	dark ppt. / carbide	72.1 ± 5.0	9.2 ±1.0	9.3 ±1.7	4.7 ±1.2	4.7 ±1.1

Table 4

Phase compositions of the $CrMnFe_{0.5}CoNi$ alloy following a 1000 h heat treatment at 700˚C and a 5000 h heat treatment at 500˚C, obtained by averaging of SEM-EDX point spectra. The phase composition of the *bcc* phase was also measured by averaging sum area spectra from STEM-EDX maps. Elemental concentrations are given in at. %, along with the standard deviation between the measurements.

Condition	Phase / structure	Cr	Mn	Fe	Co	Ni
700°C	matrix / *fcc*	23.0 ± 0.2	20.6 ± 0.2	11.2 ± 0.3	22.6 ± 0.2	22.6 ± 0.4
	light ppt. / σ	49.9 ± 1.0	12.4 ± 0.4	9.2 ± 0.4	21.2 ± 0.3	7.3 ± 0.6
	dark ppt. / *bcc*	73.5 ± 10.5	8.8 ± 2.8	4.7 ± 1.4	7.4 ± 3.0	5.6 ± 3.3
	dark ppt. / *bcc*[*]	84.8 ± 5.8	8.4 ± 3.7	2.7 ± 0.7	2.9 ± 1.8	1.2 ± 1.8
500°C	matrix / *fcc*	23.1 ± 0.1	20.4 ± 0.2	11.4 ± 0.3	22.6 ± 0.2	22.5 ± 0.2

[*] STEM-EDX

Table 5

Phase compositions of the CrMnCoNi alloy following 1000 h heat treatments at 900 and 700˚C, and 5000 h at 500˚C. Elemental quantifications were obtained by averaging EDX point spectra in SEM or by averaging sum area spectra from STEM-EDX maps. Elemental concentrations are given in at. % along with the standard deviation between the measurements.

Condition	Phase / structure	Cr	Mn	Co	Ni
900°C	matrix / *fcc*	24.7 ± 0.4	25.4 ± 0.2	25.0 ± 0.3	24.9 ± 0.3
	light ppt. / σ	50.7 ± 0.5	15.8 ± 0.6	23.5 ± 1.2	10.0 ± 1.0
700°C	matrix / *fcc*	25.4 ± 0.2	25.0 ± 0.3	24.8 ± 0.2	24.8 ± 0.2
	light ppt. / σ	52.9 ± 0.4	13.4 ± 0.1	26.1 ± 0.3	7.6 ± 0.3
	dark ppt. / *bcc*	77.7 ± 6.8	10.0 ± 2.7	6.8 ± 1.7	5.5 ± 2.5
500°C	matrix / *fcc*	25.5 ± 0.4	25.0 ± 0.3	24.9 ± 0.3	24.6 ± 0.3
	CrCo-rich / σ*	48.0 ± 2.5	9.5 ± 1.9	37.6 ± 2.4	4.9 ± 1.2
	NiMn-rich / $L1_0$*	4.0 ± 1.7	41.1 ± 2.2	7.8 ± 2.8	47.1 ± 3.8
	Cr-rich / *bcc**	83.9 ± 1.9	7.2 ± 2.5	7.1 ± 1.5	1.8 ± 0.4
	Co-rich / *fcc**	25.7 ± 3.5	12.7 ± 2.0	45.2 ± 1.8	16.4 ± 3.0

* STEM-EDX

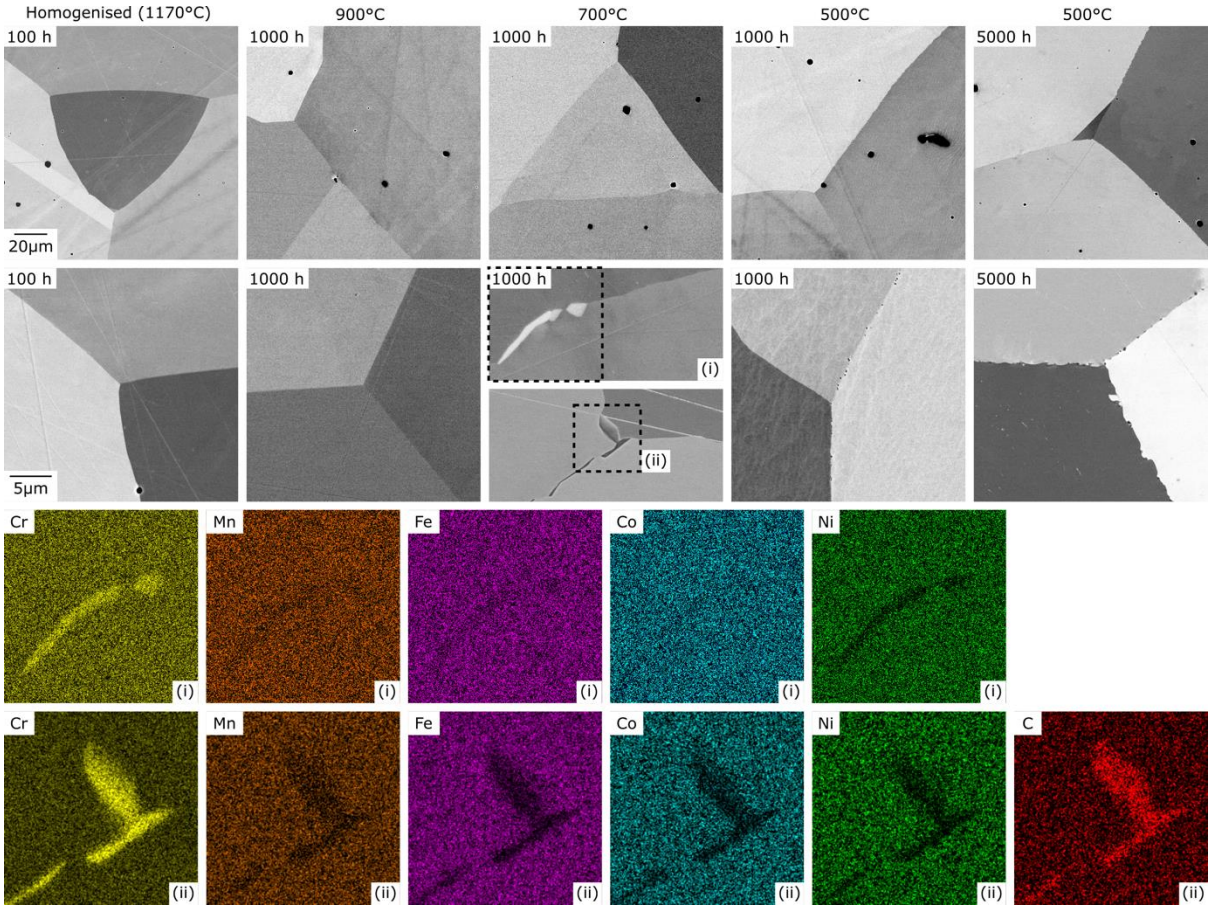

Figure 1 – BSE images of the $CrMnFe_{1.5}CoNi$ alloy in the homogenised condition, following 1000 h heat treatments at 900, 700 and 500˚C, and following an extended 5000 h exposure at 500˚C. EDX elemental partitioning maps, labelled (i) and (ii), correspond to the higher magnification BSE images of the 700˚C specimen (dashed outlines).

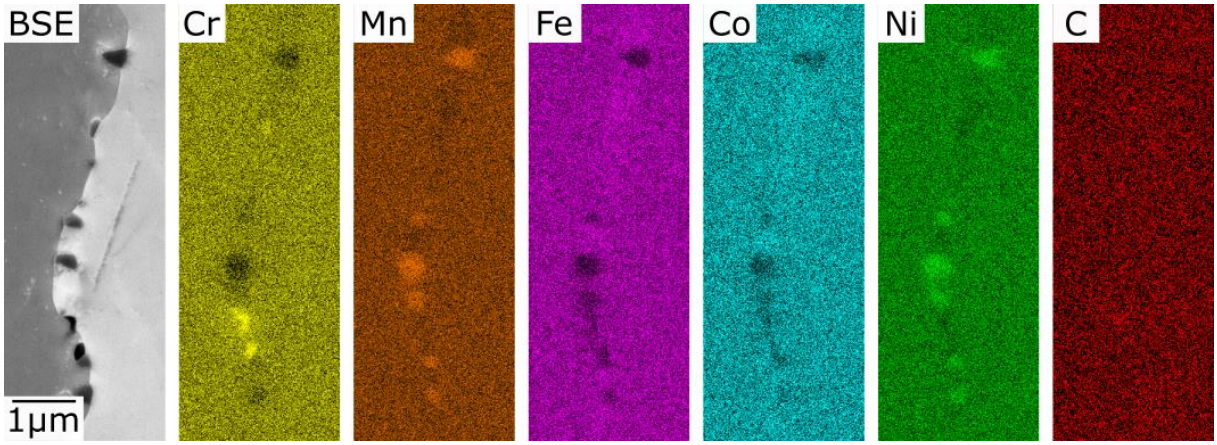

Figure 2 – BSE image and corresponding EDX elemental partitioning maps of a grain boundary region in the $CrMnFe_{1.5}CoNi$ alloy following exposure at 500˚C for 5000 h.

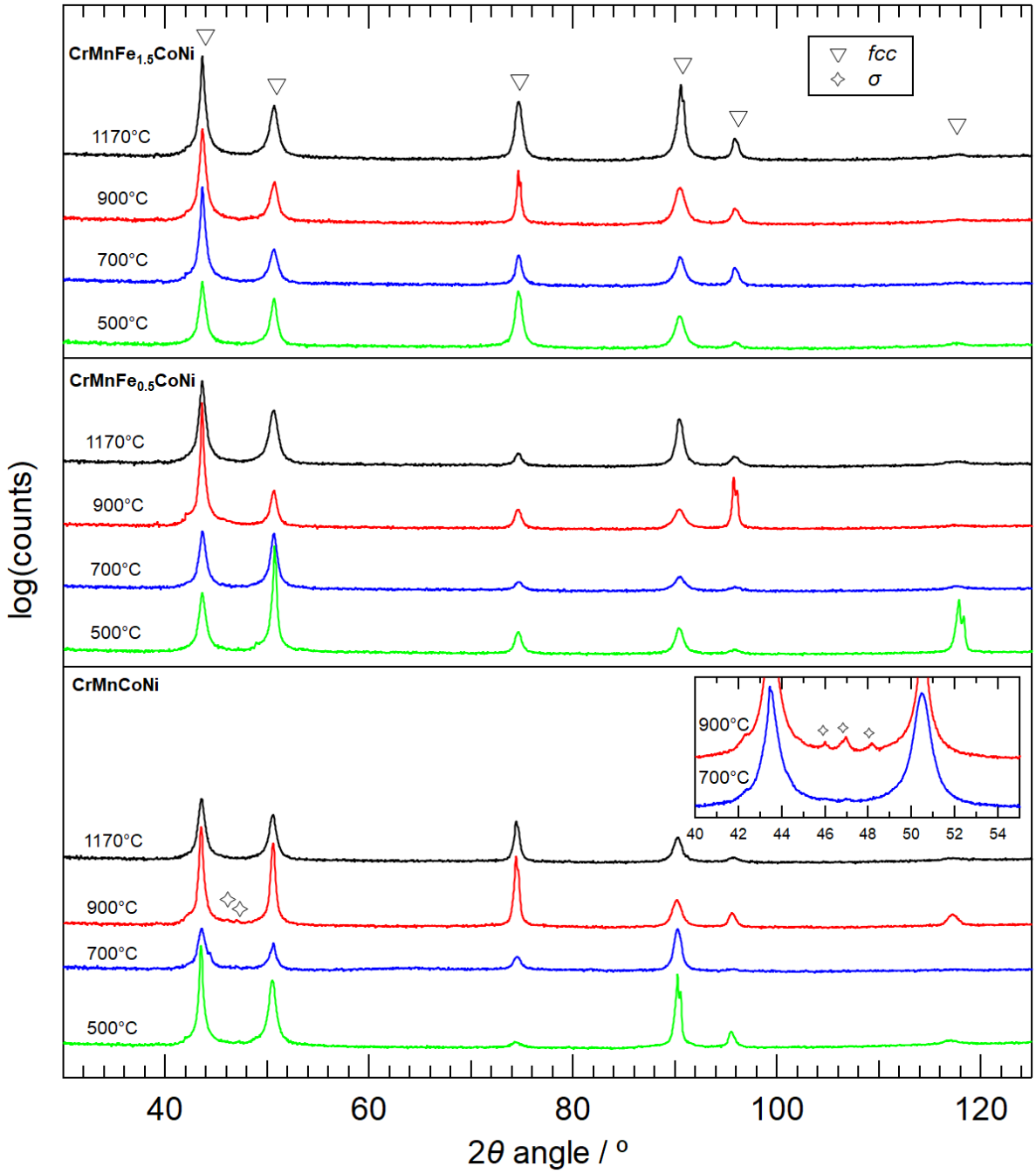

Figure 3 – XRD patterns of the $CrMnFeCo_{1.5}Ni$, $CrMnFe_{0.5}CoNi$ and CrMnCoNi alloys in the homogenised condition, and following 1000 h heat treatments at 900, 700 and 500˚C. The figure inset displays enlarged spectra from the CrMnCoNi alloy in the 900 and 700˚C conditions, following a slower scan in the angular range 40-55˚, which clearly revealed σ phase reflections in the 900˚C specimen. Please note that the apparent splitting of some peaks at high angles is simply a consequence of the separation of the $K\alpha_1$ and $K\alpha_2$ wavelengths.

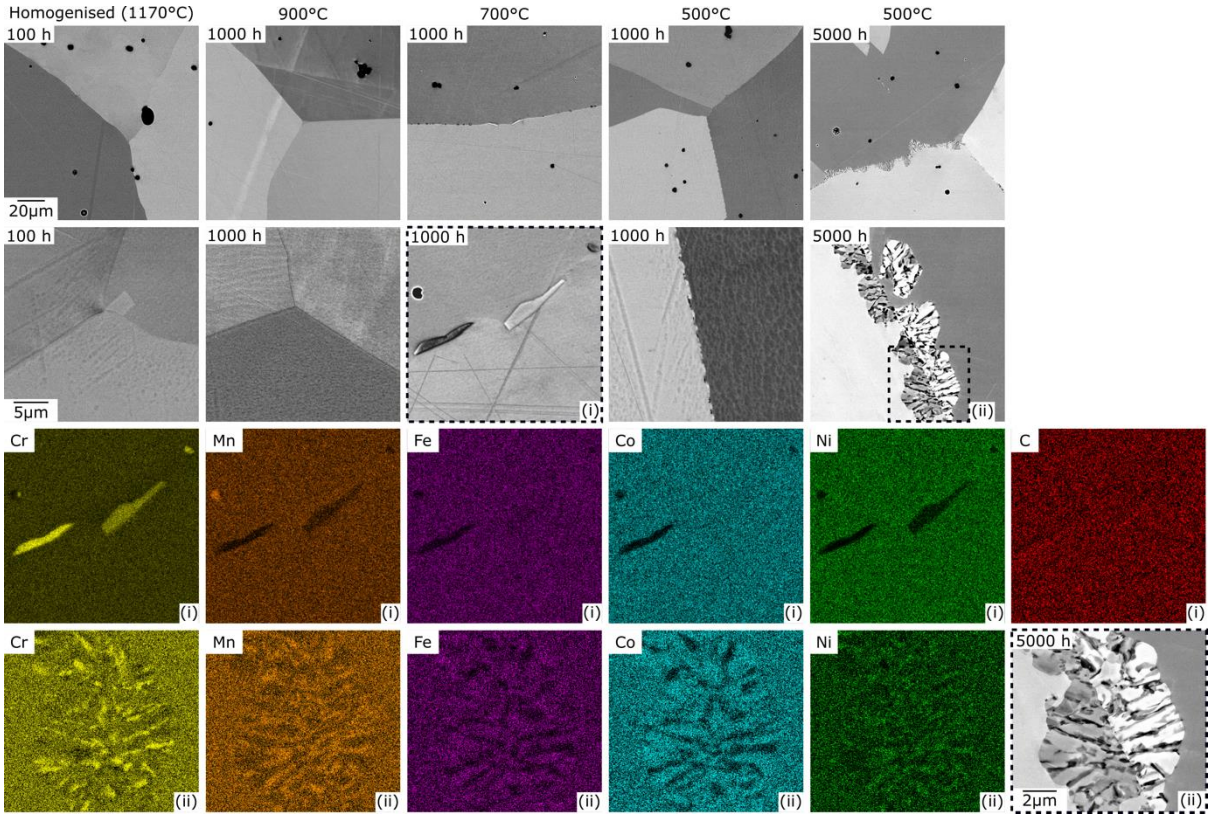

Figure 4 – BSE images of the $CrMnFe_{0.5}CoNi$ alloy in the homogenised condition, following 1000 h heat treatments at 900, 700 and 500˚C, and following an extended 5000 h exposure at 500˚C. Representative EDX elemental partitioning maps, displayed below, correspond to the dash outlined regions in the higher magnification BSE images, labelled (i) and (ii). For clarity, a high magnification BSE image of the outlined region (ii) is also shown.

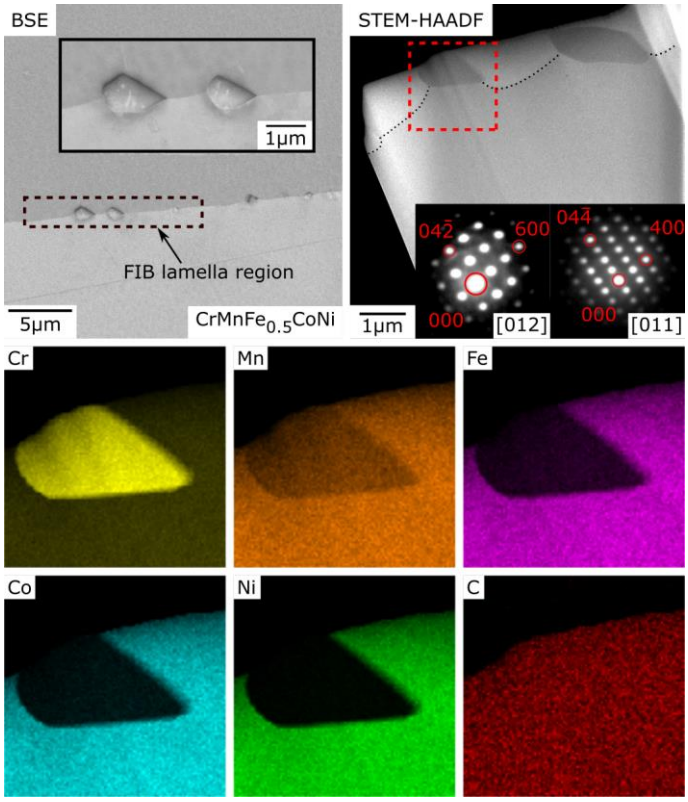

Figure 5 – BSE image of the $CrMnFe_{0.5}CoNi$ alloy shows a grain boundary region containing two dark-contrast precipitates which were extracted by FIB milling. A higher magnification BSE image of the dark-contrast precipitates is inset. Adjacent is a STEM-HAADF image of the extracted lamella, where the two dark-contrast precipitates can be seen near the top edge. For clarity, the grain boundary is delineated by a black dotted line. The STEM-EDX elemental partitioning maps, displayed below, were obtained from the red dashed region of the STEM-HAADF image. Indexed microprobe electron diffraction patterns, also obtained from the dark-contrast precipitate on the left, are inset within the STEM-HAADF image.

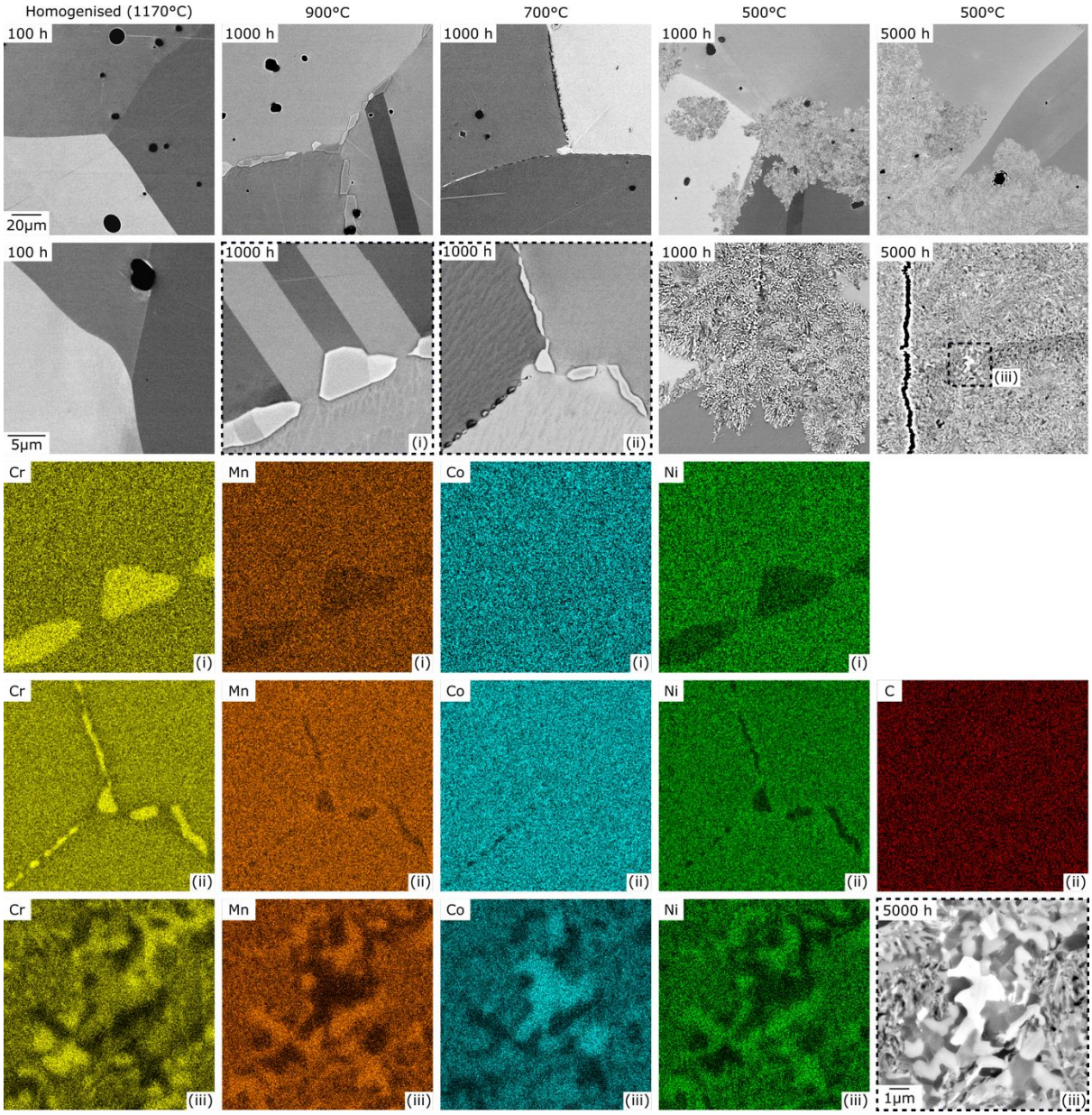

Figure 6 – BSE images of the CrMnCoNi alloy in the homogenised condition, following 1000 h heat treatments at 900, 700 and 500˚C, and after an extended 5000 h exposure at 500˚C. Representative EDX elemental partitioning maps, displayed below, correspond to the dash outlined regions in the BSE images, labelled (i) through (iii). For clarity, a high magnification BSE image of the outlined region (iii) is also shown.

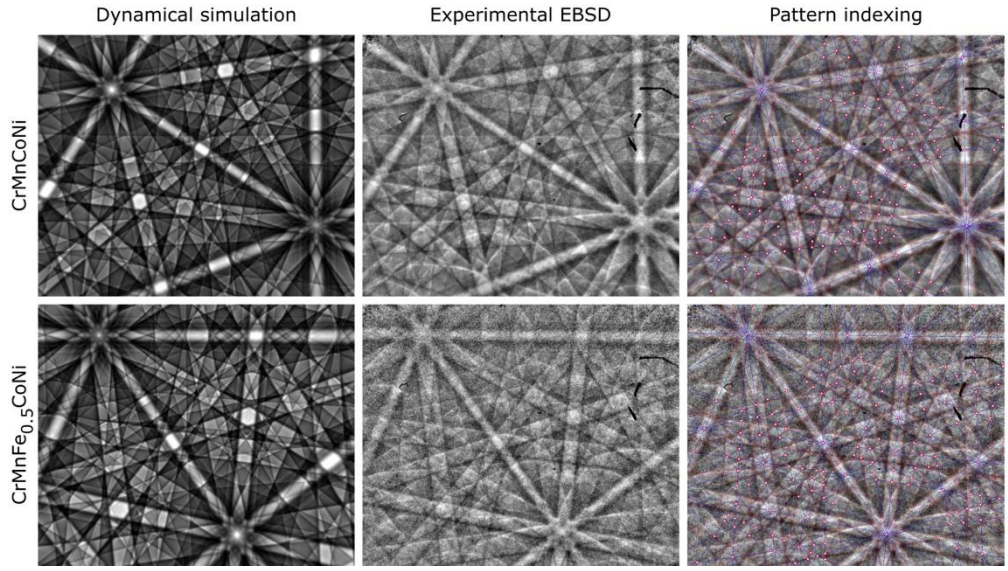

Figure 7 – EBSD patterns obtained from Cr-rich, dark-contrast precipitates in the CrMnCoNi and $CrMnFe_{0.5}CoNi$ alloys, displayed alongside dynamical simulations of the *bcc* crystal structure (a = 2.9 Å). The patterns indexed using the EBSDL program [40,41] are displayed to the right with the band centers and poles shown as blue lines and red-outlined white spots respectively.

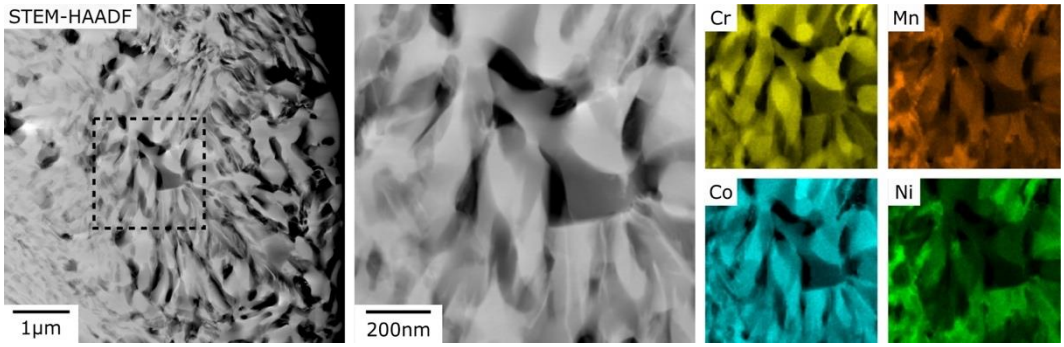

Figure 8 – STEM-HAADF images of fine-scale structures within the CrMnCoNi specimen exposed at 500˚C for 5000 h. The high-magnification image and corresponding EDX elemental partitioning maps were obtained from the dash-outlined region in the left image.

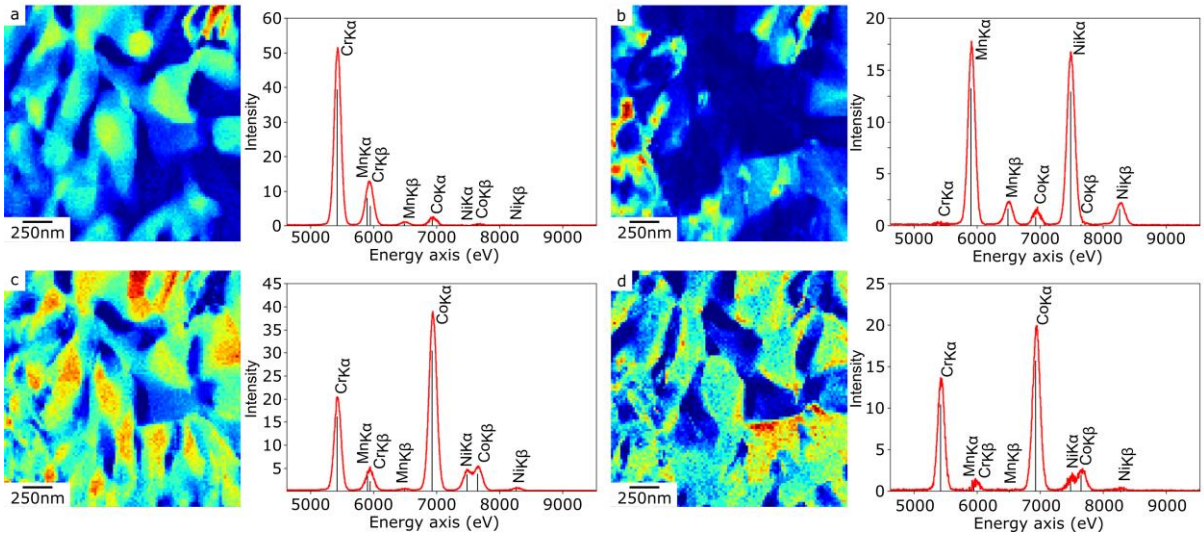

Figure 9 – Phase heat-maps and corresponding EDX spectra for four phases (a-d), identified within the CrMnCoNi alloy exposed at 500˚C for 5000 h. The four phases were identified by a principal component analysis, performed on the EDX signal from the elemental partitioning maps displayed in Fig. 8, using HyperSpy [43]. The PCA separated the spatially resolved EDX signal according to composition (spectral signal). The resulting heat-maps reveal the spatial distribution of each phase and the corresponding EDX spectra indicate the composition of each phase.

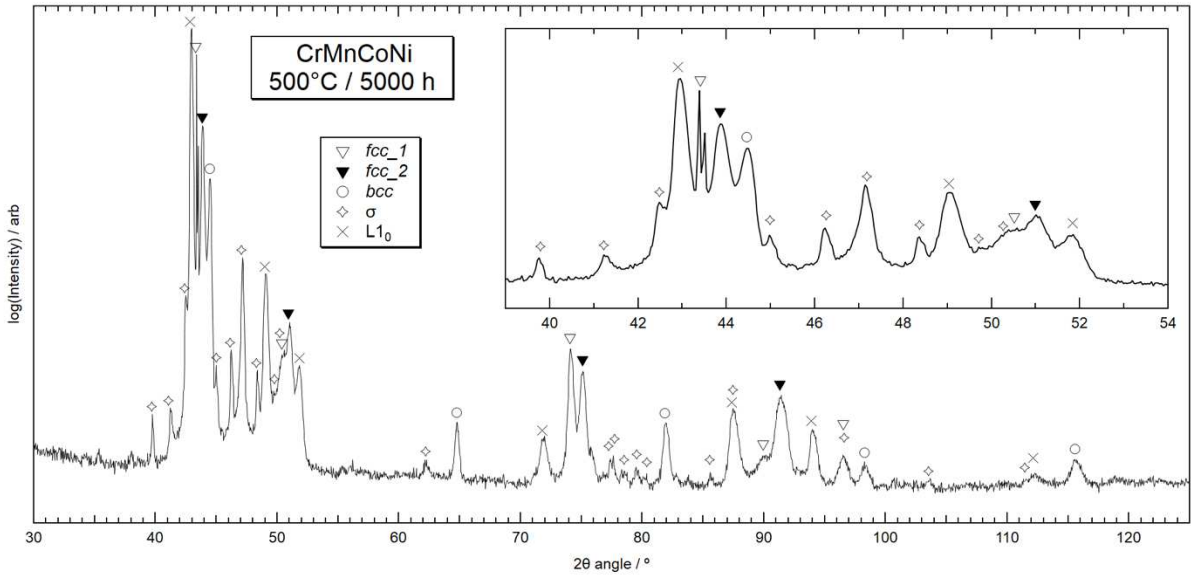

Figure 10 – XRD pattern obtained from the CrMnCoNi alloy following 5000 h heat treatment at 500˚C. The figure inset displays an enlarged region of the spectra.

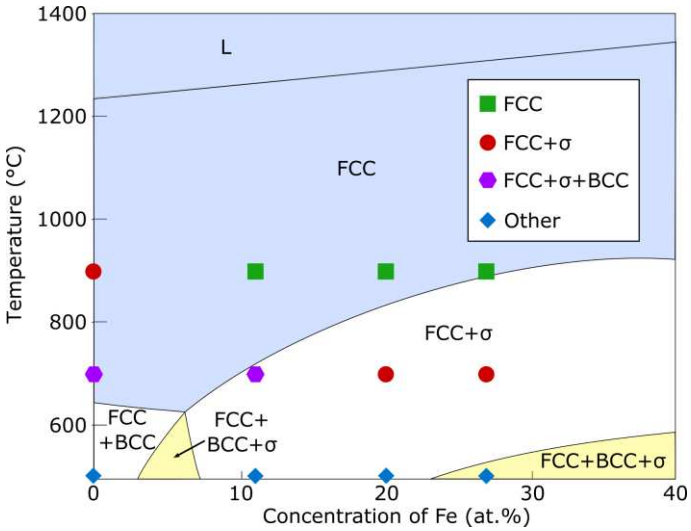

Figure 11 - Section of a Fe isopleth of the $CrMnFe_xCoNi$ alloy (where Fe is substituted equally for the other elements) showing the phase stability predictions of TCHEA3. Green squares indicate specimens which were single phase *fcc*. Compositions and temperatures where σ phase has been experimentally observed are shown as red circles and those which also contained *bcc* precipitates are denoted with purple hexagons. Blue diamonds are used for specimens which contained other phases. Experimental data for the CrMnFeCoNi alloy was obtained from the literature [6,11]. It should be noted that this diagram requires the data to be plotted using nominal, rather than actual, alloy compositions.

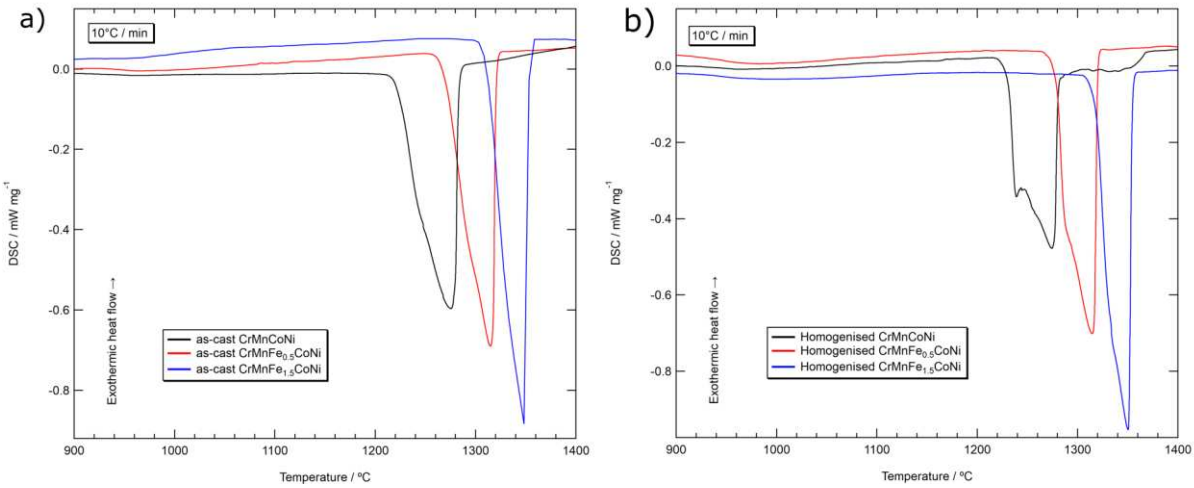

Supplementary Figure 1 – DSC traces of each alloy in the as-cast (a) and homogenized (b) conditions during heating at 10˚C / min.

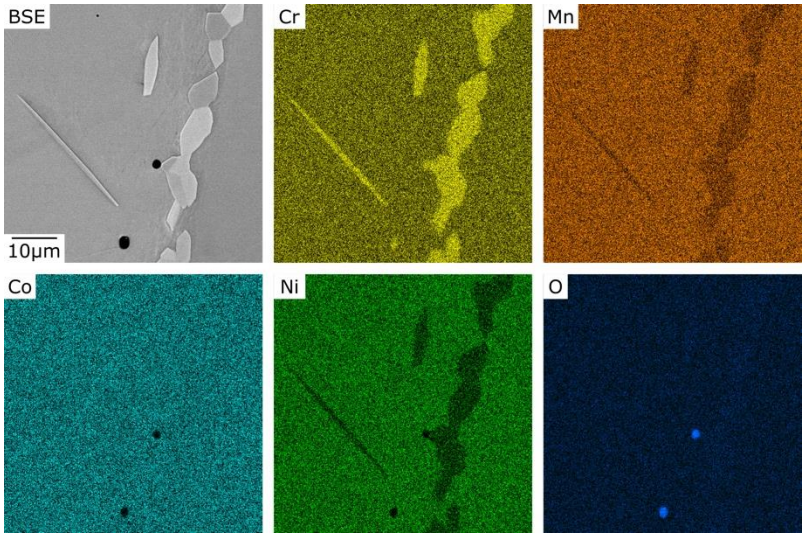

Supplementary Figure 2 – BSE image and corresponding EDX elemental partitioning maps of the CrMnCoNi alloy following heat treatment at 900˚C for 1000 h.